

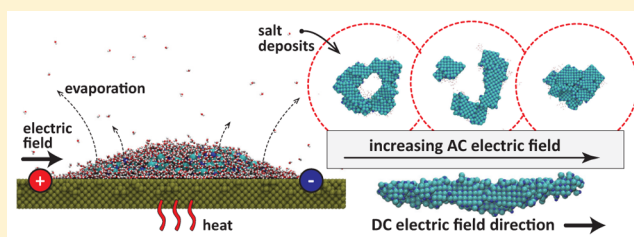
Electrowetting Controls the Deposit Patterns of Evaporated Salt Water Nanodroplets

Jun Zhang,^{*,†} Matthew K. Borg,[†] Konstantinos Ritos,[‡] and Jason M. Reese[†]

[†]School of Engineering, University of Edinburgh, Edinburgh EH9 3FB, United Kingdom

[‡]Department of Mechanical and Aerospace Engineering, University of Strathclyde, Glasgow G1 1XJ, United Kingdom

ABSTRACT: So-called “coffee-ring” stains are the deposits remaining after complete evaporation of droplets containing nonvolatile solutes. In this paper we use molecular dynamics to simulate the evaporation of salt water nanodroplets in the presence of an applied electric field. We demonstrate, for the first time, that electrowetted nanodroplets can produce various deposit patterns, which vary substantially from the original ringlike deposit that occurs when there is no electric field. If a direct current (dc) electric field with strength greater than 0.03 V/Å is imposed parallel to the surface, after the water evaporates the salt crystals form a deposit on the substrate in a ribbon pattern along the field direction. However, when an alternating current (ac) electric field is applied the salt deposit patterns can be either ringlike or clump, depending on the strength and frequency of the applied ac field. We find that an ac field of high strength and low frequency facilitates the regulation of the deposit patterns: the threshold electric field strength for the transition from ringlike to clump is approximately 0.006 V/Å. These findings have potential application in fabricating nanostructures and surface coatings with desired patterns.



INTRODUCTION

Evaporation of sessile liquid droplets containing nonvolatile solutes such as DNA, polymers, colloids, and ions on solid surfaces has many potential applications. These include DNA chip manufacturing,¹ inkjet printing,^{2,3} manufacturing of nanostructures via self-assembly of nanoparticles,^{4–6} and surface coatings.^{7,8} In these problems, the solutes deposit on a surface to form a variety of patterns toward the end of the evaporation process. The most well-known post-evaporative pattern is the so-called “coffee-ring” stain, named after the ring of residuals that is observed at the circumference of an evaporated coffee drop. Deegan et al.^{9–11} proposed that capillary flow, induced by droplet evaporation at a pinned contact line, is the main cause of the coffee-ring phenomenon. Besides ringlike deposits, central clump, uniform pancake, and multiple rings deposit patterns have also been reported in experiments.^{6,12,13}

For many applications, it is required to control both the morphology of the deposit patterns and their positions on the solid surfaces. For example, uniform deposits, rather than ringlike, are usually required in coatings of electronic and optical devices. For this reason, a number of studies have tested procedures to regulate deposit patterns, such as by thermal Marangoni flows,¹⁴ substrate patterning,⁵ and recently also by electrowetting.^{15–17}

Electrowetting uses an electric field to modify the wetting properties of droplets on surfaces, an effect that was first explained by Lippmann¹⁸ in 1875. In order to overcome the problem of electrolysis, Berge¹⁹ introduced the idea of using an insulating layer to separate the conductive liquid from the

metallic electrode; this concept is known as electrowetting on dielectric (EWOD). The contact angle θ of a droplet, with an applied external voltage U , can be described by the well-known Young–Lippmann equation²⁰

$$\cos \theta = \cos \theta_Y + \eta = \frac{\gamma_{sv} - \gamma_{sl}}{\gamma_{lv}} + \frac{\epsilon \epsilon_0 U^2}{2d\gamma_{lv}} \quad (1)$$

where θ_Y is Young’s contact angle, γ_{sv} , γ_{sl} , and γ_{lv} are the surface tensions of the solid–vapor, solid–liquid, and liquid–vapor interfaces, respectively, $\eta = \epsilon \epsilon_0 U^2 / 2d\gamma_{lv}$ is the electrowetting number, which measures the strength of the electrostatic forces with respect to the surface tension, ϵ is the dielectric constant of the insulating layer, ϵ_0 is the vacuum permittivity, and d is the thickness of the insulating layer. According to eq 1, the contact angle of a droplet decreases with the applied external voltage. This theoretical analysis has been validated by experiments up to contact angle saturation.^{21,22}

Electrowetting provides a unique way to exert forces directly to the contact line of sessile droplets. An intriguing idea is to use electrowetting to regulate the deposit patterns of evaporating droplets. Eral et al.^{15,16} have demonstrated that the ringlike pattern of colloidal particles can be suppressed by applying an alternating current (ac) electric field. Orejon et al.¹⁷ applied a direct current (dc) electric field to droplets containing nanoparticles and found a continuous and smoother receding of the contact line during evaporation. In this case, a more

Received: December 2, 2015

Revised: January 16, 2016

Published: January 20, 2016

uniform patterning of the deposit was observed, in contrast to the phenomena of pinned contact lines and ring stains without electrowetting. These experimental studies showed that electrowetting is a promising tool for regulating the deposit patterns of macroscopic droplets. Recently, continuum theoretical analysis and numerical modeling of the evaporation of particle-laden macroscopic droplets with an applied electric field have been reported by Wray et al.²³ Their results demonstrated that the ringlike deposit pattern can be suppressed using an appropriate electric field.

Interest in nanodroplets is growing because of their potential applications in manufacturing, such as creating nanostructures through evaporation. The electrowetting properties of nanodroplets are somewhat different from macroscopic droplets. An electric field can permeate the entirety of a nanodroplet, although it can be screened by liquid polarization. The competition between the spontaneous orientation of dipolar fluid molecules and the realignment caused by an electric field results in a change in surface tensions and so a change in the contact angle of the droplets. Daub et al.²⁴ investigated electrowetting of water nanodroplets using molecular dynamics (MD) simulations for the first time. More comprehensive investigations into electrowetting of pure water and salt water nanodroplets have been carried out by Yen,²⁵ Daub et al.,²⁶ and Song et al.²⁷ These results showed that the electric field could change the wetting properties of nanodroplets to some extent. However, results for evaporating nanodroplets with an applied electric field have not yet been produced.

In our previous MD study²⁸ of evaporating salt water nanodroplets with no applied electric fields, we observed two typical deposit patterns after complete evaporation: clump and ringlike—the preferred formation depending on the solid–liquid interaction strength and the evaporation rate. In the present paper, we apply electric fields during the evaporation process in order to regulate the deposit formations of salt crystals, while keeping the solid–liquid interaction strength and the evaporation rate constant. To the best of our knowledge, this is the first time that regulating the deposit patterns of evaporating nanodroplets has been investigated using electro-wetting.

■ SIMULATION MODEL AND METHOD

We perform molecular dynamics (MD) simulations of salt water nanodroplets on a platinum surface using the mdFOAM software,^{29–34} which is a highly parallelized MD solver implemented within the open source framework OpenFOAM and validated across various micro/nano flow problems. The rigid TIP4P/2005 model³⁵ is used to simulate the water molecules. This model consists of four sites: one oxygen site (no charge), two hydrogen sites ($0.5564 e$), and one massless site M ($-1.1128 e$). Hamilton's quaternions are employed to keep the fixed geometry of the water molecules. The Na^+ ($1.0 e$) and Cl^- ($-1.0 e$) ions are treated as nonpolarizable sites with fixed charges. As demonstrated in ref 36, polarization of water molecules and ions by the external field is negligible if the field strength is below 1 V/\AA . All intermolecular interactions between pairs of molecules for O, H, M, Na^+ , Cl^- , and Pt sites are based on the following combined Lennard-Jones (LJ) and Coulomb potentials:

$$u_{\alpha\beta}(r) = 4\epsilon_{\alpha\beta} \left[\left(\frac{\sigma_{\alpha\beta}}{r} \right)^{12} - \left(\frac{\sigma_{\alpha\beta}}{r} \right)^6 \right] + \frac{1}{4\pi\epsilon_0} \frac{q_\alpha q_\beta}{r} \quad (2)$$

where r is the distance between site α and site β , q_α is the partial charge of site α , $\epsilon_{\alpha\beta}$ is the well depth of the LJ potential, and $\sigma_{\alpha\beta}$ is the characteristic diameter. The LJ parameters for all sites are listed in Table 1. Coulomb interactions exist between sites with

Table 1. Lennard-Jones Potential Parameters for Atomic Sites in Water Molecules, Na^+ and Cl^- Ions, and Pt Atoms^a

site	ϵ (kJ/mol)	σ (Å)
H	0	0
O	0.775	3.1589
M	0	0
Na^+	0.196	2.45
Cl^-	0.628	4.1
Pt	66.84	2.471
H– Na^+	0.180	1.55
H– Cl^-	0.323	2.375

^aThese values are taken from refs 28, 35, and 38.

charges. Since the droplet is of finite size, and the semi-infinite solid surface carries no charges, the use of Ewald sums is not warranted.^{24,27,37} Previous studies showed that a cutoff radius of 1.2 nm can provide acceptable accuracy with computational efficiency^{28,34,37} and so is adopted in this paper.

The Lorentz–Berthelot mixing rules are used to determine the LJ cross interactions between atomic sites, except that additional LJ potential interactions for H– Cl^- and H– Na^+ are included to prevent the overestimation of ion hydration.³⁸ The modified LJ potential parameters for H– Cl^- and H– Na^+ pairs are also listed in Table 1. Interactions between the platinum surfaces and the droplets are based on the Lorentz–Berthelot mixing rules for Pt–O, Pt– Na^+ , and Pt– Cl^- pairs, with an extra scaling parameter of 0.38 that determines the droplet wetting property on the surface. For this choice of scaling parameter, the equilibrium contact angles of pure water droplets and salt water droplets with a concentration of 25.1% are 0° and 36.1° , respectively, as demonstrated in our previous paper.²⁸

The MD simulation box is 18.8 nm in the x and z directions (parallel to the solid surface) and 31.4 nm in the y direction (perpendicular to the solid surface). Periodic boundary conditions are applied in all three directions. We set up each simulation by first initializing 4832 pure water molecules as well as 500 Na^+ and 500 Cl^- ions in a simple lattice and placing it on a platinum surface with an fcc structure (lattice constant 3.92 Å). The atoms in the bottom four layers of the platinum surface are fixed, while the atoms in the top four layers are coupled to a Berendsen thermostat to control their temperature. The integration time step is 2 fs. The MD system is run for 4 ns of problem time at 300 K to reach an equilibrium state. The salt water cube relaxes into a droplet during this period (as shown in Figure 1), with a contact angle of 36.1° and a contact radius of 6.43 nm.

After the system reaches equilibrium, we induce evaporation by linearly increasing the temperature of the platinum surface to 600 K in 4 ns. During this period, liquid water molecules in the droplets continuously evaporate to vapor, while all Na^+ and Cl^- ions remain part of the droplet, thus increasing the salt concentration and ultimately reaching saturation, at which point salt crystals deposit on the surface. Our previous study²⁸ showed that a ringlike pattern was formed for these conditions (without an applied electric field).

In this paper we focus on a possible way to change the deposit patterns from ringlike to ribbon or clump using

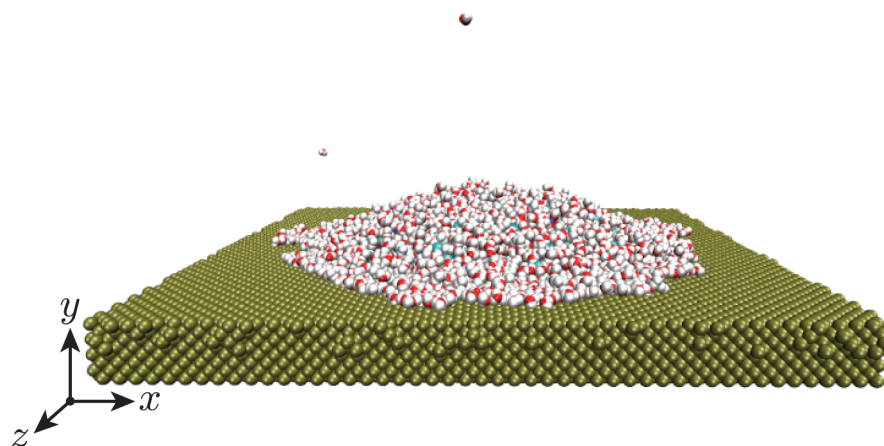


Figure 1. Snapshot of a salt water droplet on a platinum surface (at 300 K) at an equilibrium state without an applied electric field.

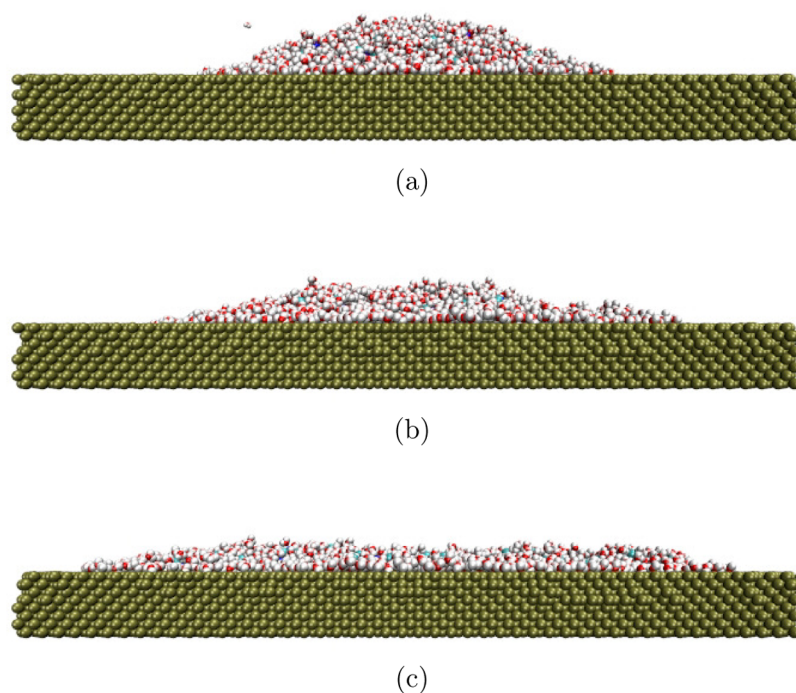


Figure 2. Side view of salt water droplets on platinum surfaces after 4 ns of problem time: (a) without an electric field; (b) $E_x = 0.01$ V/Å; (c) $E_x = 0.05$ V/Å. For droplets with an applied electric field, the morphology along the long sides is shown.

electrowetting. Two types of electric fields are applied parallel to the surface in separate simulation cases: a dc field ($E_x = E_0$) and an ac field ($E_x = E_0 \cos(2\pi ft)$ together with $E_z = E_0 \sin(2\pi ft)$), where f is the frequency and E_0 is the strength of the field. A phase difference of 90° between the x and z directions in the ac field ensures the effect of the electric field on a droplet is axisymmetric in a complete period. Having the electric fields parallel to the surface in our simulations corresponds to a recent electrowetting experiment,¹⁵ where interdigitated electrodes were placed on substrates along a horizontal direction; this was instead of the conventional electrowetting technique that immerses a wire into the droplet.²⁰ In our simulations, the field is implemented as an additional force $\vec{F}_E = q_i \vec{E}$ to all charged sites i in the MD system. For the simulation cases with an applied dc field, the electric field is applied to the system from the start of the simulation, in order to change the wetting properties of the droplets before the substrate is heated. For the simulation cases with an applied ac field, the electric

field is applied when the surface temperature starts rising, i.e., from a problem time of $t = 4$ ns.

RESULTS AND DISCUSSION

Evaporation in the Presence of a DC Electric Field. We first investigate the wetting properties of a salt water droplet with a dc electric field applied along the x direction in order to validate our results and also to initialize a steady state droplet under an externally applied field. Figure 2 shows snapshots of salt water droplets in our simulations after 4 ns of problem time. The contact angle is determined by fitting the liquid–vapor interface to a truncated circle.^{28,37} Without an electric field applied (Figure 2a), the equilibrium contact angle is about 36.1° . With increasing electric field strength, the droplet elongates in the direction of the field (Figure 2b), and the contact angle on the long sides of the droplet decreases accordingly. This phenomenon is consistent with MD simulation results reported by Daub et al.²⁴ for pure water

droplets and by Daub et al.²⁶ and Song et al.²⁷ for salt water droplets. This phenomenon is also consistent with the experimental results of Restolho et al.,²² Shapiro et al.,³⁹ Quinn et al.,⁴⁰ and Brassard et al.⁴¹ before contact angle saturation is reached. When the electric field is greater than 0.03 V/Å, the salt water droplet stretches into a molecularly thin high-aspect-ratio ribbon, almost completely wetting the surface (Figure 2c).

We now simulate evaporation with an applied dc electric field of various strengths. The temperature of the platinum surface is increased from 300 to 600 K in 4 ns of problem time. Because of the heat transfer between the platinum surface and the droplet, the temperature of the droplet increases and water molecules escape from the condensed liquid phase to become vapor. We count a water molecule as part of the vapor phase if it has fewer than 10 water molecule neighbors within a distance of 6.3 Å.²⁸ For the remainder of this section we discuss the results of the 0.05 V/Å case, since higher field strengths produce similar deposits and fields lower than 0.03 V/Å produce ringlike deposits (just as in cases without an electric field²⁸). Figure 3 shows the temporal evolution of the number

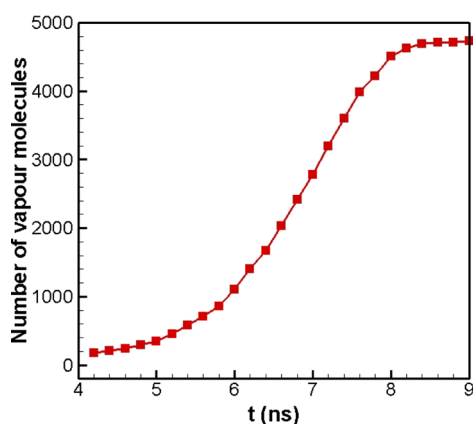


Figure 3. Temporal evolution of the number of water vapor molecules in the evaporation process. The surface temperature is raised from 300 to 600 K in the period 4–8 ns.

of vapor molecules. When the problem time reaches 8.6 ns, almost all the water molecules have become vapor and the remaining salt ions deposit on the surface.

Figure 4 shows top views of the salt ions at various stages in the simulation when the electric field strength is 0.05 V/Å; the

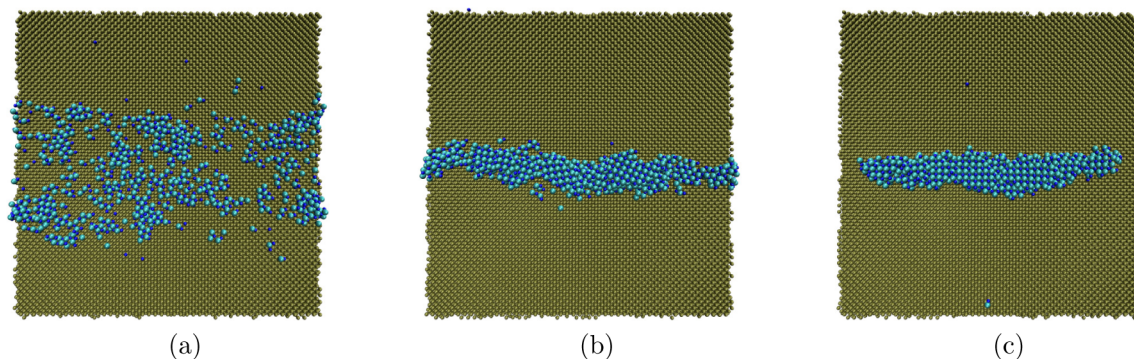


Figure 4. Top view of salt ions on the platinum surface during the evaporation process when $E_x = 0.05$ V/Å: (a) $t = 4$ ns (at the equilibrium state); (b) $t = 6.6$ ns; (c) $t = 9.0$ ns. Chloride ions are cyan, sodium ions are blue, and platinum atoms are olive-green.

platinum atoms are also included in order to show the positions of salt ions relative to the surface, while water molecules have been excluded to make these figures more clear. Figure 4a shows the distribution of salt ions within the stretched droplet. Once evaporation begins, small clusters form due to the electrostatic force between salt ions, and these small clusters may merge to form larger clusters. The electric field has an orientating effect, and the salt clusters prefer to align themselves along the field direction (Figure 4b). Finally, salt crystals with a ribbonlike pattern are deposited on the surface (Figure 4c). The length of the ribbon is about 15.0 nm, and the width is 3.2 nm. If the simulation box and the salt water droplet are larger, we expect to obtain longer ribbons at similar conditions. These results suggest that evaporating droplets containing nonvolatile solutes in the presence of an external dc field is a promising way to fabricate high-aspect-ratio nanowires.

Evaporation in the Presence of an AC Electric Field.

Applying an ac field parallel to the surface may influence the dynamic aggregation of ions within a droplet during the evaporation process, and consequently the final deposit pattern. We apply an ac electric field to the simulation system in the same way as in the dc cases, but with time-varying components in both the x and z directions: $E_x = E_0 \cos(2\pi ft)$ and $E_z = E_0 \sin(2\pi ft)$. Each MD simulation case starts from the equilibrium state (after 4 ns of problem time) without an applied field. The ac field is then imposed on the system, and the temperature of the surface is raised. In these simulations we carry out a two-dimensional parametric study of the effects of electric field strength E_0 and ac frequency f on the deposited patterns of salt. The electric field strengths chosen range from 0.005 to 0.02 V/Å, while the ac frequency is in the range 10–100 GHz. The period of the ac field is selected to be time scale separated from the features in the problem: around 1 order of magnitude larger than the characteristic time scale of the molecular motion (i.e., 1 ps) and 1 order of magnitude smaller than the time scale of the evaporation process (i.e., 4 ns).

Figure 5 provides an overview of the deposit patterns of salt water nanodroplets after complete evaporation for the various electric field strengths and frequencies we tested. There are two distinguishable regimes (typical of nanodroplet evaporation studies²⁸): ringlike deposits (denoted by empty circles) and clump deposits (filled circles). A linear relationship, of the form $f = 7500E_0 - 45$, distinguishes between the two patterns within the range of electric fields and frequencies tested in this paper. It is also evident that a correlation may exist between the obtained deposit pattern and the electric field applied, allowing

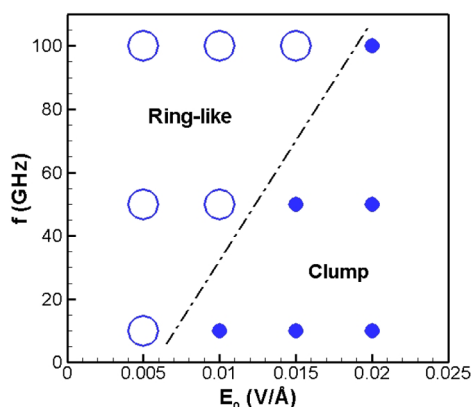


Figure 5. Deposit patterns of salt water nanodroplets after complete evaporation: ac electric fields parallel to the surface are imposed with different strengths (E_0) and frequencies (f). A ringlike deposit is denoted by a large empty circle, while a clump pattern is denoted by a small filled circle.

the transition between ringlike and clump by means of adjusting the field parameters. For example, the ringlike pattern that is ubiquitous for various particle-laden droplets with long evaporation periods without an applied electric field²⁸ can instead be a clump pattern for the same evaporating droplet if the strength of the applied ac field is increased. This transition phenomenon from ringlike to clump using an electric field is similarly observed in the experiments of Eral et al.^{15,16} and Orejon et al.,¹⁷ although the nanodroplets used in our MD simulations are 6 orders of magnitude smaller than the millimeter-sized droplets used in their experiments. Our simulations also indicate that an increase in ac frequency may increase this critical transition electric field strength.

To further investigate this phenomenon, we compare the temporal evolution of the liquid–vapor interface in two cases: $E_0 = 0.005$ V/Å (ringlike) and $E_0 = 0.01$ V/Å (clump), both at 10 GHz frequency. As shown in Figure 6, there are three stages observed in the evaporation process. The first occurs from 4.0 to 4.6 ns, during which the evaporation rate is slow and the droplets spread out slightly due to the increase in temperature. This stage is almost the same as the equivalent case without an applied electric field.²⁸ The second stage is from 4.6 to 5.4 ns, during which the evaporation becomes quicker, but the liquid–vapor interface remains pinned at the contact line. This is a result of capillary flow from the center of the droplet toward its perimeter to replenish the liquid molecules lost in evaporation,

as shown in Figure 7. The two simulated cases are qualitatively similar in this second stage; however, the magnitude of the capillary flow in the droplet with $E_0 = 0.01$ V/Å is smaller than the case with $E_0 = 0.005$ V/Å, as is evident when comparing the velocity fields in Figure 7a,b. This indicates that an ac electric field with higher strength impedes the formation of the capillary flow. There are more obvious differences in the third stage (after 5.4 ns), during which the droplet with $E_0 = 0.01$ V/Å shrinks along the surface much faster than the droplet with $E_0 = 0.005$ V/Å.

Typical snapshots of the evaporation process for $E_0 = 0$ V/Å (the no electric field case included for comparison from ref 28) and 10 GHz ac fields with $E_0 = 0.005$ V/Å and $E_0 = 0.01$ V/Å are shown in Figures 8a–d, 8e–h, and 8i–l, respectively. Chloride ions are cyan, and sodium ions are blue. The black dashed circles denote the perimeters of the droplets at the initial equilibrium, and the small red dots are liquid water molecules. Figures 8a,e,i are the starting configurations at which heating of the substrate begins. As the droplets heat, they spread out during the first two stages due to the capillary flow, as shown in Figures 8b,f,j. Note that the capillary flow for $E_0 = 0.005$ V/Å is stronger than for $E_0 = 0.01$ V/Å (Figure 7), so more salt ions aggregate and form small clusters in the region close to the rim of the droplet in the former case (Figure 8f) than the latter case (Figure 8j). In the third stage, as the droplets shrink, salt ions start to move inward accordingly. The salt concentration in the region close to the contact line keeps increasing as more free salt ions are absorbed into clusters, and this generates a pinning force along the contact line. As a result, the recession of the contact line becomes slower. When $E_0 = 0.005$ V/Å, the salt ions hardly move after 6.4 ns (Figure 8g) and finally deposit as a ringlike pattern (Figure 8h). Note that both complete and partial ringlike patterns are possible, and the formation of one rather than the other is somewhat random and depends on the initial conditions. On the other hand, when $E_0 = 0.01$ V/Å, the stronger electric force can overcome the pinning force, so the salt ions continuously move inward during the third stage (Figure 8k) and finally deposit as a clump in the center (Figure 8l). For all three cases, after complete evaporation there are still a few water molecules adsorbed on the surface of the salt crystals. The desorption and adsorption of water molecules on surfaces are in dynamic equilibrium, while the salt crystals maintain their structures.

Based on the above analysis, in order to form clump patterns the electric force must surpass the pinning force in the shrink stage. In the following we estimate the threshold strength of the

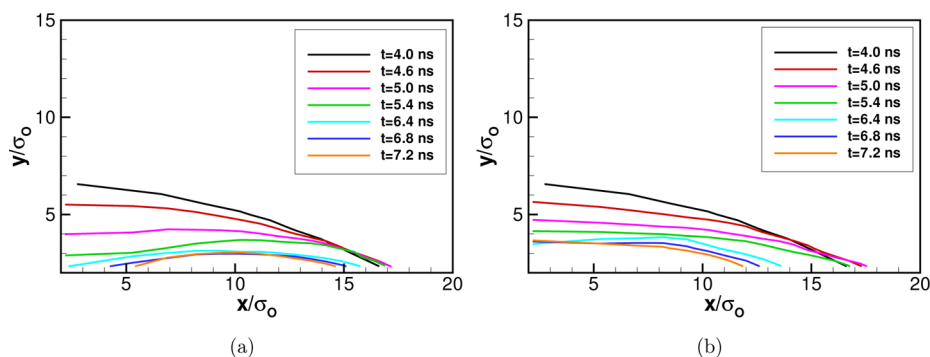


Figure 6. Temporal evolution of the droplet liquid–vapor interface during the evaporation process with applied ac electric fields of frequency 10 GHz: (a) $E_0 = 0.005$ V/Å; (b) $E_0 = 0.01$ V/Å. The coordinates are normalized by σ_0 (the characteristic diameter of the oxygen site in water molecules).

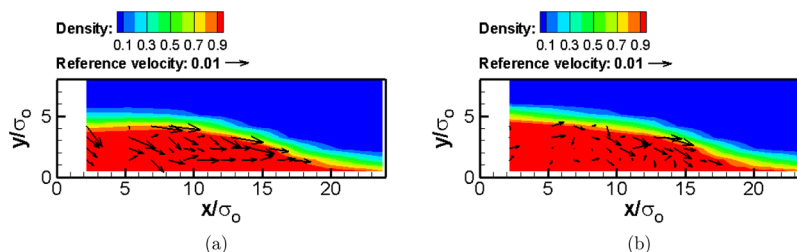


Figure 7. Normalized density contours and velocity vectors (black arrows) at $t = 4.8$ ns with applied ac electric fields of frequency 10 GHz: (a) $E_0 = 0.005$ V/Å; (b) $E_0 = 0.01$ V/Å. The density and velocity are normalized by σ_0^{-3} and $(\epsilon_0/m_0)^{1/2}$, respectively.

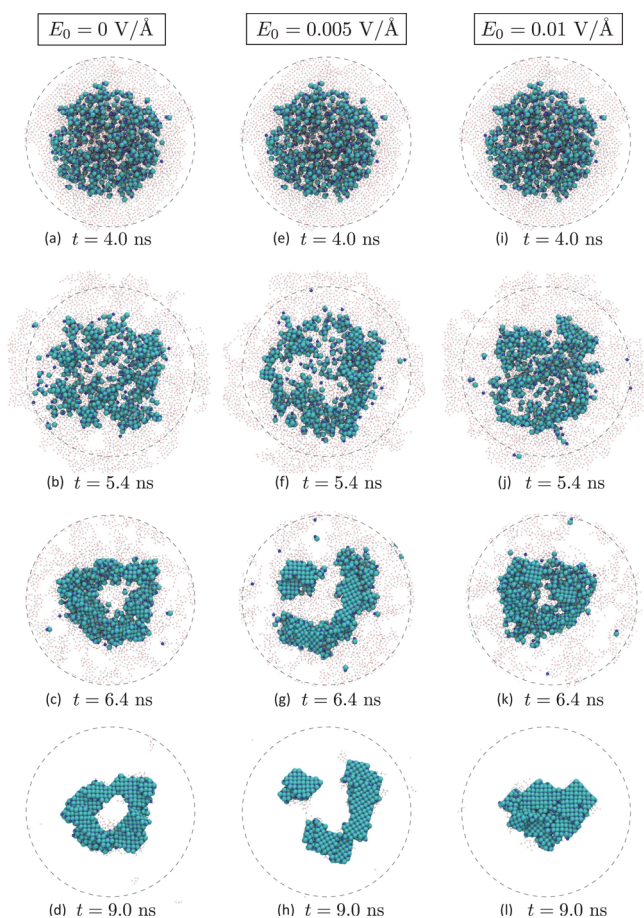


Figure 8. Top view of the salt ions in nanodroplets during the evaporation process. The first column is the case without an electric field, taken from ref 28, which is included here for comparison. Columns 2 and 3 are snapshots from the 10 GHz ac electric field cases with $E_0 = 0.005$ V/Å and $E_0 = 0.01$ V/Å, respectively. Chloride ions are cyan, and sodium ions are blue. The black dashed circles denote the perimeters of the droplets at the initial equilibrium, and the small red dots are water molecules.

ac field, above which the deposit pattern changes from ringlike to clump. According to electrowetting theory,²⁰ the electric force f_{el} is

$$f_{el} = \frac{\epsilon\epsilon_0 E_0^2 \cos^2(2\pi ft)d}{2} + \frac{\epsilon\epsilon_0 E_0^2 \sin^2(2\pi ft)d}{2} = \frac{\epsilon\epsilon_0 E_0^2 d}{2} \quad (3)$$

where ϵ (the dielectric constant) has a saturated value of about 45 for salt water of high concentration,⁴² and d can be considered to be the characteristic diameter of the droplet at

the shrink stage. The strength of the pinning force f_p is related to the contact angle hysteresis,¹⁵ i.e.

$$f_p \approx \gamma_V (\cos \theta_a - \cos \theta_r) \quad (4)$$

where γ_V is the surface tension of salt water, and $\cos \theta_a$ and $\cos \theta_r$ are the advancing and receding contact angles, respectively. Although it is difficult to obtain accurate values of $\cos \theta_a$ and $\cos \theta_r$, a rough estimation gives 0.1 for $\cos \theta_a - \cos \theta_r$.

By comparing f_{el} in eq 3 with f_p in eq 4, we find that if E_0 is larger than 0.006 V/Å, the electric force surpasses the pinning force, and the deposit pattern is likely to change to a clump pattern. This outline calculation is in agreement with our simulation results in Figure 5.

The frequency of the electric field also plays an important role. Figure 9 shows the temporal evolution of the droplet liquid–vapor interface during the evaporation process when the field strength is constant (0.01 V/Å) but for two different frequencies (50 and 100 GHz). Comparing with the 10 GHz case in Figure 6b, it is evident that in the third stage of the evaporation process (i.e., after 5.4 ns) a higher applied ac frequency slows the receding motion of the droplet along the surface. At higher frequencies, the time scale of the periodically varying electrophoretic force becomes comparable to the local equilibration time scale, which as a result reduces the effect of the applied electric field and enables the original ringlike pattern to deposit on the surface. For the salt water nanodroplets considered in this paper, we have shown that to ensure the deposit pattern is a uniform clump rather than ringlike, ac electric fields of high strength and low frequency should be applied.

CONCLUSIONS

We have used molecular dynamics to investigate the evaporation of salt water nanodroplets when an electric field is applied. Our previous studies of the same droplet had shown that without an electric field the salt ions form a ringlike pattern after complete evaporation of the water. Here we have focused on the control of the deposit pattern using electrowetting: our simulations have demonstrated, for the first time, that it is feasible to change the deposit pattern from ringlike to ribbon using a dc electric field parallel to the surface, and from ringlike to clump using an ac electric field parallel to the surface (depending on the ac frequency and field strength). These findings not only shed light on the mechanisms of electrowetting in regulating deposit patterns but also have potential application to the fabrication of nanostructures and surface coatings with desired patterns or structures. Research on the phase change dynamics of electrowetted nanodroplets containing other types of nonvolatile solutes, such as DNA, polymers, and colloids, would be useful future work.

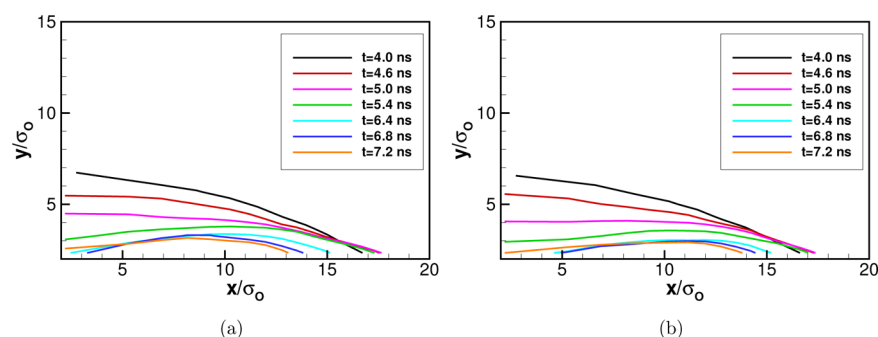


Figure 9. Temporal evolution of the droplet liquid–vapor interface during the evaporation process, with an applied ac electric field of 0.01 V/Å and different frequencies: (a) 50 GHz and (b) 100 GHz. These frequencies produce ringlike patterns, as is evident from the evolution of the interface. Refer to Figure 6b for comparison with the 10 GHz case that produces a clump pattern.

AUTHOR INFORMATION

Corresponding Author

*E-mail: zhangjun04@foxmail.com (J.Z.).

Notes

The authors declare no competing financial interest.

ACKNOWLEDGMENTS

This work is financially supported by the UK's Engineering and Physical Sciences Research Council (EPSRC) under Grants EP/I011927/1, EP/K038621/1, and EP/N016602/1. Results were obtained using the ARCHIE-WeSt High Performance Computer, under EPSRC Grants EP/K000586/1 and EP/K000195/1. All data within this publication can be freely accessed at: <http://dx.doi.org/10.7488/ds/1321>.

REFERENCES

- Dugas, V.; Broutin, J.; Souteyrand, E. Droplet evaporation study applied to DNA chip manufacturing. *Langmuir* **2005**, *21*, 9130–9136.
- Tekin, E.; Smith, P. J.; Schubert, U. S. Inkjet printing as a deposition and patterning tool for polymers and inorganic particles. *Soft Matter* **2008**, *4*, 703–713.
- De Gans, B.-J.; Duineveld, P. C.; Schubert, U. S. Inkjet printing of polymers: state of the art and future developments. *Adv. Mater.* **2004**, *16*, 203–213.
- Brinker, C. J.; Lu, Y.; Sellinger, A.; Fan, H. Evaporation-induced self-assembly: nanostructures made easy. *Adv. Mater.* **1999**, *11*, 579–585.
- Vakarelski, I. U.; Chan, D. Y.; Nonoguchi, T.; Shinto, H.; Higashitani, K. Assembly of gold nanoparticles into microwire networks induced by drying liquid bridges. *Phys. Rev. Lett.* **2009**, *102*, 058303.
- Bhardwaj, R.; Fang, X.; Somasundaran, P.; Attinger, D. Self-assembly of colloidal particles from evaporating droplets: role of DLVO interactions and proposition of a phase diagram. *Langmuir* **2010**, *26*, 7833–7842.
- Kistler, S. F.; Schweizer, P. M. *Liquid Film Coating*; Chapman & Hall: 1997.
- Brutin, D. *Droplet Wetting and Evaporation: From Pure to Complex Fluids*; Elsevier: 2015.
- Deegan, R. D.; Bakajin, O.; Dupont, T. F.; Huber, G.; Nagel, S. R.; Witten, T. A. Capillary flow as the cause of ring stains from dried liquid drops. *Nature* **1997**, *389*, 827–829.
- Deegan, R. D. Pattern formation in drying drops. *Phys. Rev. E: Stat. Phys., Plasmas, Fluids, Relat. Interdiscip. Top.* **2000**, *61*, 475.
- Deegan, R. D.; Bakajin, O.; Dupont, T. F.; Huber, G.; Nagel, S. R.; Witten, T. A. Contact line deposits in an evaporating drop. *Phys. Rev. E: Stat. Phys., Plasmas, Fluids, Relat. Interdiscip. Top.* **2000**, *62*, 756.
- Shmuylovich, L.; Shen, A. Q.; Stone, H. A. Surface morphology of drying latex films: multiple ring formation. *Langmuir* **2002**, *18*, 3441–3445.
- Bhardwaj, R.; Fang, X.; Attinger, D. Pattern formation during the evaporation of a colloidal nanoliter drop: a numerical and experimental study. *New J. Phys.* **2009**, *11*, 075020.
- Hu, H.; Larson, R. G. Marangoni effect reverses coffee-ring depositions. *J. Phys. Chem. B* **2006**, *110*, 7090–7094.
- Eral, H. B.; Augustine, D. M.; Duits, M. H.; Mugele, F. Suppressing the coffee stain effect: how to control colloidal self-assembly in evaporating drops using electrowetting. *Soft Matter* **2011**, *7*, 4954–4958.
- Mampallil, D.; Eral, H.; van den Ende, D.; Mugele, F. Control of evaporating complex fluids through electrowetting. *Soft Matter* **2012**, *8*, 10614–10617.
- Oregon, D.; Sefiane, K.; Shanahan, M. E. Evaporation of nanofluid droplets with applied DC potential. *J. Colloid Interface Sci.* **2013**, *407*, 29–38.
- Lippmann, G. Relations entre les phénomènes électriques et capillaires Ph.D. Thesis, Gauthier-Villars, 1875.
- Berge, B. Electrocapillarity and wetting of insulator films by water. *C. R. Acad. Des. Sci., Ser. II* **1993**, *317*, 157–163.
- Mugele, F.; Baret, J.-C. Electrowetting: from basics to applications. *J. Phys.: Condens. Matter* **2005**, *17*, R705.
- Lin, J.-L.; Lee, G.-B.; Chang, Y.-H.; Lien, K.-Y. Model description of contact angles in electrowetting on dielectric layers. *Langmuir* **2006**, *22*, 484–489.
- Restolho, J.; Mata, J. L.; Saramago, B. Electrowetting of ionic liquids: Contact angle saturation and irreversibility. *J. Phys. Chem. C* **2009**, *113*, 9321–9327.
- Wray, A. W.; Papageorgiou, D. T.; Craster, R. V.; Sefiane, K.; Matar, O. K. Electrostatic suppression of the “coffee stain effect”. *Langmuir* **2014**, *30*, 5849–5858.
- Daub, C. D.; Bratko, D.; Leung, K.; Luzar, A. Electrowetting at the nanoscale. *J. Phys. Chem. C* **2007**, *111*, 505–509.
- Yen, T.-H. Investigation of the effects of perpendicular electric field and surface morphology on nanoscale droplet using molecular dynamics simulation. *Mol. Simul.* **2012**, *38*, 509–517.
- Daub, C. D.; Bratko, D.; Luzar, A. Electric control of wetting by salty nanodrops: Molecular dynamics simulations. *J. Phys. Chem. C* **2011**, *115*, 22393–22399.
- Song, F.; Li, B.; Liu, C. Molecular Dynamics Simulation of the Electrically Induced Spreading of an Ionically Conducting Water Droplet. *Langmuir* **2014**, *30*, 2394–2400.
- Zhang, J.; Borg, M. K.; Sefiane, K.; Reese, J. M. Wetting and evaporation of salt-water nanodroplets: A molecular dynamics investigation. *Phys. Rev. E* **2015**, *92*, 052403.
- Macpherson, G. B.; Reese, J. M. Molecular dynamics in arbitrary geometries: parallel evaluation of pair forces. *Mol. Simul.* **2008**, *34*, 97–115.
- Borg, M. K.; Macpherson, G. B.; Reese, J. M. Controllers for imposing continuum-to-molecular boundary conditions in arbitrary fluid flow geometries. *Mol. Simul.* **2010**, *36*, 745–757.

- (31) Nicholls, W.; Borg, M. K.; Lockerby, D. A.; Reese, J. M. Water transport through carbon nanotubes with defects. *Mol. Simul.* **2012**, *38*, 781–785.
- (32) Borg, M. K.; Lockerby, D. A.; Reese, J. M. A multiscale method for micro/nano flows of high aspect ratio. *J. Comput. Phys.* **2013**, *233*, 400–413.
- (33) Borg, M. K.; Lockerby, D. A.; Reese, J. M. Fluid simulations with atomistic resolution: a hybrid multiscale method with field-wise coupling. *J. Comput. Phys.* **2013**, *255*, 149–165.
- (34) Ritos, K.; Dongari, N.; Borg, M. K.; Zhang, Y.; Reese, J. M. Dynamics of nanoscale droplets on moving surfaces. *Langmuir* **2013**, *29*, 6936–6943.
- (35) Abascal, J. L.; Vega, C. A general purpose model for the condensed phases of water: TIP4P/2005. *J. Chem. Phys.* **2005**, *123*, 234505.
- (36) Yang, K.-L.; Yiacoymi, S.; Tsouris, C. Canonical Monte Carlo simulations of the fluctuating-charge molecular water between charged surfaces. *J. Chem. Phys.* **2002**, *117*, 337–345.
- (37) Werder, T.; Walther, J. H.; Jaffe, R.; Halicioglu, T.; Koumoutsakos, P. On the water-carbon interaction for use in molecular dynamics simulations of graphite and carbon nanotubes. *J. Phys. Chem. B* **2003**, *107*, 1345–1352.
- (38) Alejandre, J.; Chapela, G. A.; Bresme, F.; Hansen, J.-P. The short range anion-H interaction is the driving force for crystal formation of ions in water. *J. Chem. Phys.* **2009**, *130*, 174505.
- (39) Shapiro, B.; Moon, H.; Garrell, R. L.; Kim, C.-J. Equilibrium behavior of sessile drops under surface tension, applied external fields, and material variations. *J. Appl. Phys.* **2003**, *93*, 5794–5811.
- (40) Quinn, A.; Sedev, R.; Ralston, J. Contact angle saturation in electrowetting. *J. Phys. Chem. B* **2005**, *109*, 6268–6275.
- (41) Brassard, D.; Malic, L.; Normandin, F.; Tabrizian, M.; Veres, T. Water-oil core-shell droplets for electrowetting-based digital micro-fluidic devices. *Lab Chip* **2008**, *8*, 1342–1349.
- (42) Hasted, J.; Ritson, D.; Collie, C. Dielectric properties of aqueous ionic solutions. Parts I and II. *J. Chem. Phys.* **1948**, *16*, 1–21.